STScI | SPACE TELESCOPE SCIENCE INSTITUTE

WFC3 Instrument Science Report 2019-07

WFC3/IR Photometric Repeatability

V. Bajaj

June 4, 2019

Abstract

The infrared channel of Wide Field Camera 3 (WFC3) on the Hubble Space Telescope (HST) is frequently used to obtain precision photometric measurements. We investigate the repeatability of WFC3 infrared (WFC3/IR) photometry by analyzing repeated observations of local stellar clusters and star forming regions. In general, the 1σ repeatability for aperture photometry is ±1.5%, even with (included) Poisson noise well under 1%. The repeatability seems to be affected by persistence of previous exposures, which can mostly be alleviated by dithering to previously unused positions, with a spacing of at least 10 pixels between positions. Observations taken this way have a much better 1σ repeatability limit of 0.5% (when Poisson noise is much smaller than 1%). The repeated measurements of standard white dwarf stars used in the absolute photometric calibration show a spread of σ = 1.5%, (Poisson noise is approximately 0.5%, indicating the repeatability is also affected by persistence) so the calibration will be improved by taking observations with a more advantageous dither strategy.

Introduction

The ability of the Hubble Space Telescope (HST) to conduct precision photometry is one of the many reasons why HST has been so scientifically productive for the last quarter century. The WFC3/IR channel uses a 1kx1k Teledyne HgCdTe detector and is sensitive to near-IR wavelengths. Knowing the overall photometric repeatability (the photometric precision) of WFC3/IR is a necessary step in understanding the quality of both relative and absolute photometry, as the zeropoints are computed by repeated measurements of photometric standard stars (isolated, non-variable stars, typically white dwarfs).

Using images of stellar clusters and star forming regions that have been imaged multiple times over short timescales (on the order of an HST orbit) we can estimate how repeatable WFC3/IR photometric measurements are. A phenomenon known as persistence occurs after pixels on the detector have been exposed to sources that fill up significant fractions of the full well depth (full well is approximately 78000e^-). Persistence manifests as an afterglow of the bright objects from previous exposures. The overall effect of persistence depends on a few parameters, including the brightness of the sources that cause it. Since stellar clusters feature many stars of varying brightness, they can be used to determine if persistence strongly impacts photometric repeatability. The repeatability can then be compared to the measurements of a standard star such as GD-153 (used in the absolute photometric calibration) to determine if persistence also effects these measurements.

Cluster Data

Stellar clusters feature many sources of varying brightness in a single exposure, so multiple exposures of the same cluster provide a vast number of experiments to test repeatability. Aperture photometry performed on sources common to multiple exposures measures the repeatability directly, and helps mitigate noise to see overall trends in the repeatability.

The MAST Archive was searched for WFC3/IR imaging data of star forming regions and stellar clusters (both open and globular clusters), and datasets with the following qualities were selected and downloaded for this study. Since the aim of the study was to measure short-term repeatability the datasets had to have multiple exposures of a given field taken in the same filter/filters (wide or medium band only), similar exposure times for images in the same filter, and similar exposure start times (ideally within the same visit). Most of the data chosen was taken using the F160W filter, as it is one of the most used filters, shows good long-term stability, has a fairly large bandpass (high signal) and is not affected by the upper atmosphere's helium emission line. The requirement of similar exposure start times helps remove effects of other factors such as calibration file changes, long-term changes to the spacecraft itself, and astrophysical variable stars. While higher source density in the images provides more measurements, the relatively large pixel scale (.13"/pixel) of the WFC3/IR detector results in poor angular resolution, making aperture photometry in crowded fields less accurate. Thus only fields with a limited degree of crowding were used, throwing out some of the more observed fields such as those in the galactic bulge and ω Cen. The fields used in this investigation are listed below.

Field	RA, Dec	Type	Dithers	Program
CB130	274.068, -2.544	Star Forming	≈8", Infrequent	11618
Messier 4	245.924, -26.505	Globular Cluster	≈0.5", Frequent	12602
NGC 1850	77.173, -68.723	Super Star Cluster	None	11933

Table 1: Fields analyzed in this investigation. The fields cover a variety of cluster types. See the appendix for more information on each target, including the individual exposure information.

Methods

All exposures (`*flt.fits` filles) for a single target/filter pair were combined together using AstroDrizzle into a single `drz.fits` file. To ensure optimal combination, the data were aligned to the Gaia DR2 catalog using the process described by Bajaj (2017). After alignment, the images were drizzled at the nominal pixel scale (.13"/pixel), with no shrinking of the input pixels (`pixfrac=1`). This is to try to make the DRZ image the most similar to the FLT images as possible. The resulting drizzled image is a pixel-wise average of the input images (corrected for bad pixels and other artifacts) and was used as a reference image to compare to the input FLT measurements.

Sources were found in one of the DRZ images (typically the F160W image was chosen) for each field using the `find_peaks()` function in the Python package PhotUtils (Bradley et al. (2017)). Thresholds for the source detection were chosen to select as many sources as possible, while not also detecting false positives (such as diffraction spikes of brighter stars). The detected sources were then recentered by calculating the centroid of small cutout of the image around each detected source. Performing the source finding on the drizzled image gave more accurate centroid positions. Coordinates of the detections were then transformed to the frame of the input FLT files using the functions `all_pix2world()` and `all_world2pix()` in the `astropy.wcs` package (The Astropy Collaboration et al. (2018)).

The final source positions were then used as the positions for the circular photometric apertures. An aperture size of 3 pixels (0.4", the standard photometric aperture) was used to capture as much light as possible while minimizing contamination from other sources within the aperture. Photometry was performed on both the DRZ and FLT images and the value obtained in the DRZ image was used as a reference. The aperture sums were computed by the PhotUtils function `aperture_photometry()`. The fluxes were background subtracted by computing the sigma-clipped mode ($3 \times median - 2 \times mean$) of an annulus at 9 pixels with a width of 3 pixels (dimensions were chosen to well outside the PSF wings, while limiting contamination from neighboring sources). The background subtracted fluxes were then converted to instrumental magnitudes. Any stars with negative fluxes were rejected, as this indicates a poor flux or background measurement.

By comparing the measurement of a single star in the DRZ image to its measurements from the FLT frames an estimation of the photometric precision can be made. Normalizing the measurements (i.e. DRZ mag - FLT mag) allows for analysis across a range of magnitudes. Computing the standard deviation of the FLT magnitudes of a single star is a direct measurement of the repeatability.

Results

Each of the detected stars' photometry and error measurements (Poisson and background noise) were calculated and compared across all of the FLT images in which that star appeared. We compare the standard deviation of the photometric measurements to the median of the calculated photometric errors for each star for each of the fields. This allows the theoretical signal-to-noise to be related to the actual dispersion of measurements.

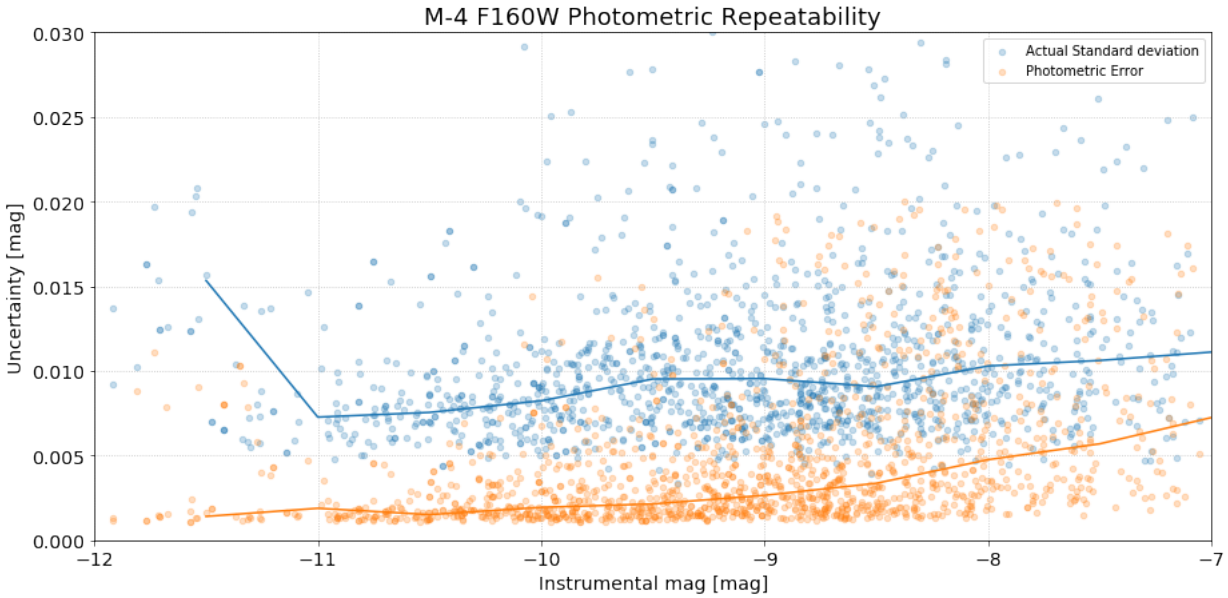

Figure 1: Comparison of the median photometric error and the standard deviation of measurements in M4 as a function of instrumental magnitude. The blue points are the standard deviation of the measurements, and the orange points are the median of the photometric error. The solid lines are the medians in half-magnitude bins.

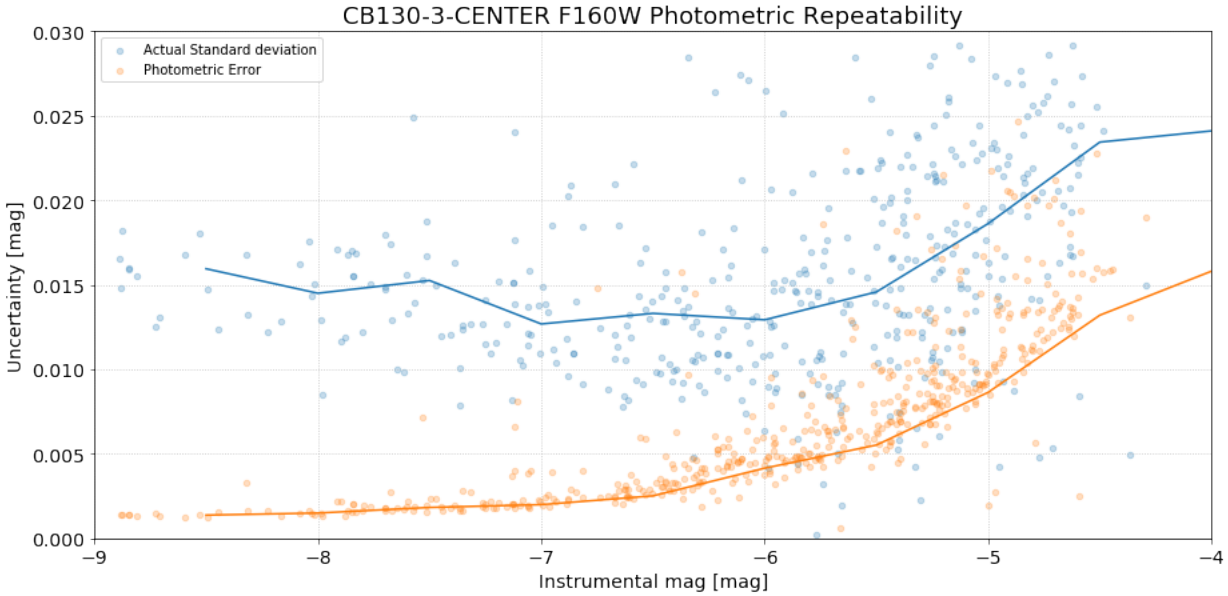

Figure 2: Comparison of the median photometric error and the standard deviation of measurements in CB130 as a function of instrumental magnitude. The blue points are the standard deviation of the measurements, and the orange are the median of the photometric error. The solid lines are the medians in half-magnitude bins.

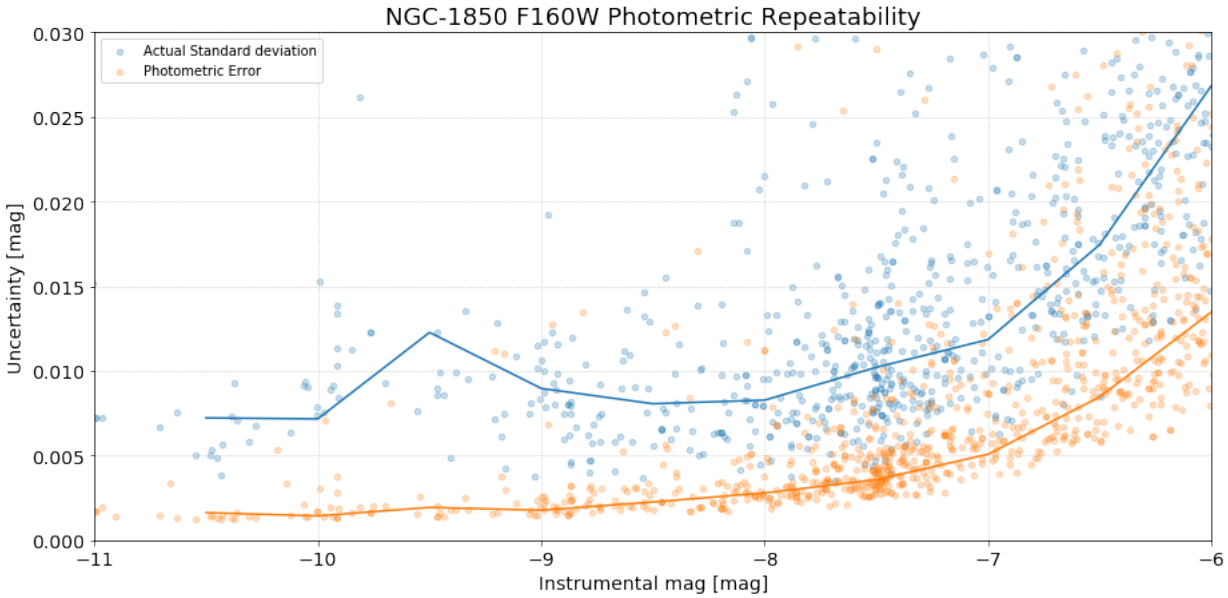

Figure 3: Comparison of the median photometric error and the standard deviation of measurements in NGC 1850 as a function of instrumental magnitude. The blue points are the standard deviation of the measurements, and the orange are the median of the photometric error. The solid lines are the medians in half-magnitude bins.

In general, the standard deviation of the FLT photometric measurements for a given star is two to three times larger than the error calculated by the photometry. This is partially due to the underestimate of the error from the background computation. The error, σ, is computed using the same formulation as IRAF's DAOPHOT. The overall flux error is calculated as:

$$\sigma^2 = \sigma_P^2 + \sigma_{BG}^2$$

Where σ_P is the Poisson noise from the source (equivalent to the square root of the aperture sum), and σ_{BG} is the error in the final flux measurement due to background subtraction. The background subtraction error term is defined:

$$\sigma_{BG}^2 = N_{ap} \times \sigma_{ann}^2 + N_{ap}^2 \times \sigma_{ann}^2 / N_{ann}$$

Where N_{ap} is the number of pixels in the photometric aperture, σ_{ann} is the standard deviation of the pixel values in the background annulus, and N_{ann} is the number of pixels in the background annulus.

While this does underestimate the error from the sky subtraction, the standard deviation of the photometric measurements is much higher than the expected error, too large to be explained solely by background error. Furthermore, the discrepancy is still large for the brighter stars, which are dominated by Poisson noise. Saturation cannot account for the large scatter either, as the full well depth for even a single pixel allows for a higher signal to noise (smaller σ) than the observed standard deviation.

To further analyze the lower than expected precision the overall photometry for each individual FLT image is compared to the DRZ photometry. By computing a sigma-clipped

median of the difference between the DRZ and FLT magnitudes for all of the stars in the FLT image, the nature of the cause of the high standard deviation can be further examined for systematic effects such as persistence.

Mitigating Persistence via Dithering

The observations of each field had different observing strategies in terms of dithering, and as a result were affected by persistence to varying degrees. Persistence causes the standard deviation of the photometric measurements to be larger by increasing the observed countrates in later images. An analysis of persistence in ω Centauri is described in Long, Baggett, and Kozhurina-Platais (2016), however, those observations were not dithered. Since dithering is strongly recommended for photometric observations, the effect of persistence on these data are not representative of typical observations. In this section we analyze the interplay between dithering and persistence effects on photometry.

M4 (Small, Frequent Dithering)

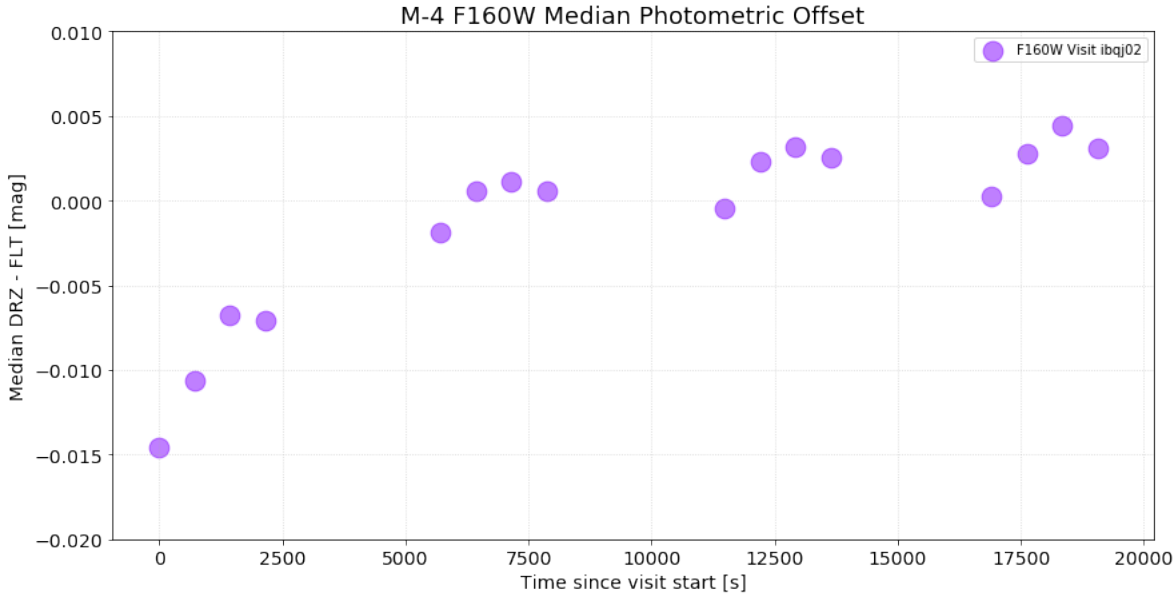

Figure 4: The median Δmag (DRZ - FLT mag) for all stars in an FLT image of M4. Each point represents a single exposure. The x value of a point represents the amount of time between the start of the visit (the exposure start of the first exposure in that visit) and the start of that exposure.

As seen in Figure 4, the observed countrates measured in the images generally increases over the visit, similar to the increase seen in Long, Baggett, and Kozhurina-Platais (2016), indicating that these data are still affected by persistence, despite the dithering. The box dither pattern used in the observations of M4 gave a spacing of approximately 4.5 pixels between dither positions in each of the four sets of exposures. While this distance is larger

than the aperture radius of 3 pixels (which should move the central/brightest pixel out of the aperture in the next image), persistence caused by the wings of the PSF from one exposure still falls within the aperture in the following exposure. Additionally the 4 point dither pattern is exactly repeated, and so all exposures from the fifth and onward reuse positions where stars had been previously, causing an increased persistence effect.

While the peak-to-peak difference is about 0.02 magnitudes (roughly 2%), the effects level off as more exposures are taken, as more of the charge traps are filled. Thus, the last orbit sees a variation of about .005 magnitudes (0.5%). However, as persistence effects decay with time, the photometry would return to the original levels if the detector pixels were not exposed to high fluence levels.

CB130 (Large, Infrequent Dithering)

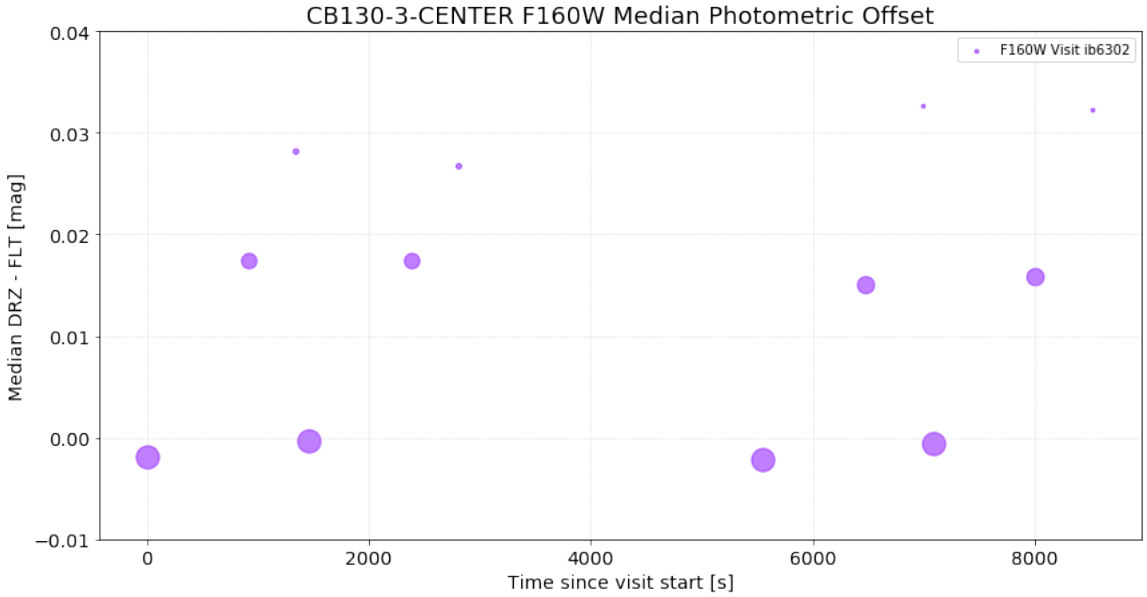

Figure 5: The median Δmag (DRZ - FLT mag) for all stars in an FLT image of CB130. Each point represents a single exposure. The size of each point is proportional to the exposure time of each image. The x value of a point represents the amount of time between the start of the visit (the exposure start of the first exposure in that visit) and the start of that exposure.

The observations of CB130 were taken in a groups of three, with a large, box-like dither (over 60 pixels) being performed after the third exposure. No other dithering was performed. This leaves the first exposure of each group virtually unaffected by persistence, as the large dither moves sources far away from previously used pixels. However, This causes persistence of the first exposure to have the substantial effect on the second exposure, and then an even larger effect from the first and second exposures on the third. The peak-to-peak difference exceeds 3% in this case, due to the use of the same pixels, and the shortest exposures being taken after the longer ones (thus giving the greatest fluence in the previous exposures,

strengthening persistence). However, the consistent level of the first (lowest) point of each group of three shows a repeatability of better than 0.5%.

NGC1850 (No Dithering)

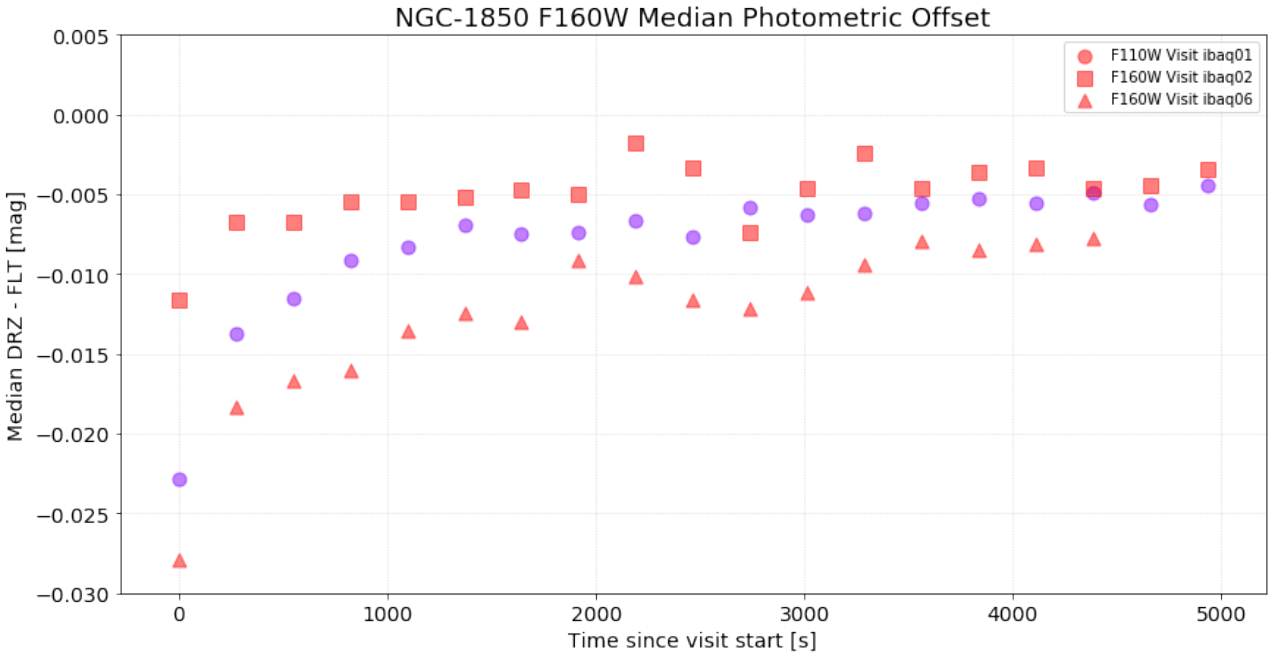

Figure 6: The median Δmag (DRZ - FLT mag) for all stars in an FLT image of NGC1850. Each point represents a single exposure. The various colors correspond to different filters, while the various symbols indicate different visits. The x value of a point represents the amount of time between the start of the visit (the exposure start of the first exposure in that visit) and the start of that exposure. Note, measurements from both F160W and F110W are included in this figure, with F110W shown in purple circles.

The observations of NGC1850 were taken in three separate (in time), one-orbit visits (though the target was in the continuous viewing zone, allowing for much more consecutive images without occultation). No dithering was performed. The effects of persistence are obvious in these exposures, with all three visits showing the same rise, then leveling off. The peak-to-peak difference for a single orbit is approximately 2.5%, consistent with the CB130 observations. The offset between the triangles and squares shows a systematically higher flux for stars in Visit 06. This is likely due to filling of charge traps from previous observations, giving rise to a lesser amount of persistence already impacting the first exposure of Visit 06.

Standard Star Photometry

The absolute photometric calibration of WFC3/IR is calculated using aperture photometry measurements of spatially isolated, non-variable standard stars. These observations are

typically taken in single-orbit visits packed with many exposures, across many different filters. Because these stars are relatively bright (for HST sensitivity) and the exposure times are often set to achieve a signal-to-noise ratio larger than 100 (though not so long to cause saturation), persistence is likely also present in these exposures. Over 900 observations of the photometric standard white dwarf GD-153 have been performed using WFC3/IR imaging modes, more than any of the other standard stars. All of the WFC3/IR images for the standard star GD-153 were downloaded (see appendix for more information), and aperture photometry was performed on the images in the same way as described in the methods section above (though only the one star of interest was measured in each image).

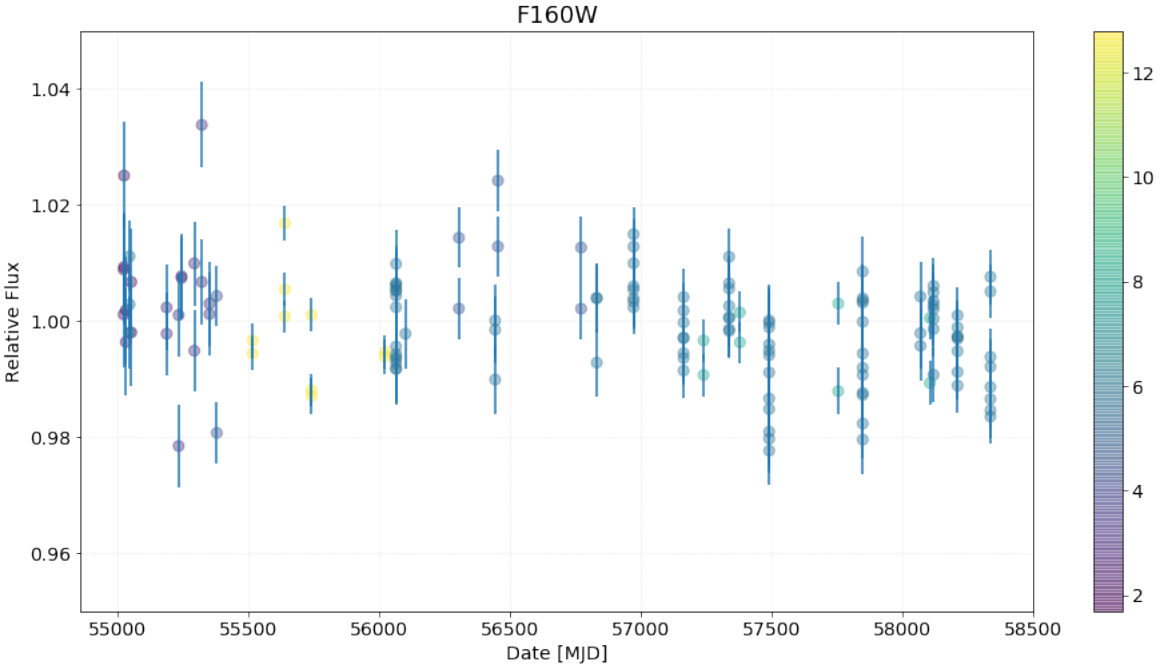

Figure 7: Aperture photometry measurements of the spectrophotometric standard star GD-153 measured over several years by WFC3/IR in the F160W filter. The 1.00 line on the y axis corresponds to the median value FLT measurements. Each point represents a single exposure of the star, and the various colors/colorbar represent the exposure time of the observation. The error bars are the computed Poisson and background error of the photometry (and does not include other noise terms such as calibration uncertainty).

As shown in Figure 7 the measurements of the standard calibration star GD-153 show a large scatter of approximately $\pm 1.5\%$. The relatively wide scatter seen for observations taken with proximity in time is on the order of the scatter seen in the clusters analyzed in previous sections. While relative photometry of a single star is more affected by Poisson noise than the cluster measurements presented above, the overall scatter is larger than the Poisson, background, and calibration noise terms for these observations (approximately 1%). This indicates a number of these observations are likely also affected by persistence, as many of the observations also had minimal distance or no dithering between exposures. More recent observations of the standard stars have adopted an observation strategy using frequent,

larger dithers of around 10 pixels, which should decrease the spread in the data, allowing for a more precise absolute photometric calibration.

This effect is difficult to see in a single visit, as it is not the dominant noise term (in figures 4, 5, and 6 hundreds of stars were measured to reduce effects of Poisson noise). However, the effects of the dithering are still apparent if many images across visits are analyzed. By normalizing the measured fluxes of the star to the median measured flux for the corresponding filter, measurements in all filters across many visits can be compared simultaneously. The pixel coordinates where the star was located in each image were recorded and transferred from local subarray coordinates to physical detector coordinates to remove effects of changing subarray size between images. For each visit the images were sorted into chronological order. For each image i in a visit, the distance between the star's (x, y) position in image i and star's position in each of the previous images in the visit was computed. The minimum of the distances was then recorded. This minimum reflects how far a dither position is from any previous dither position in the same visit.

By comparing the median/standard deviation of the normalized fluxes to the dither separation, the effects of dithering can be investigated for more than 900 observations of GD-153.

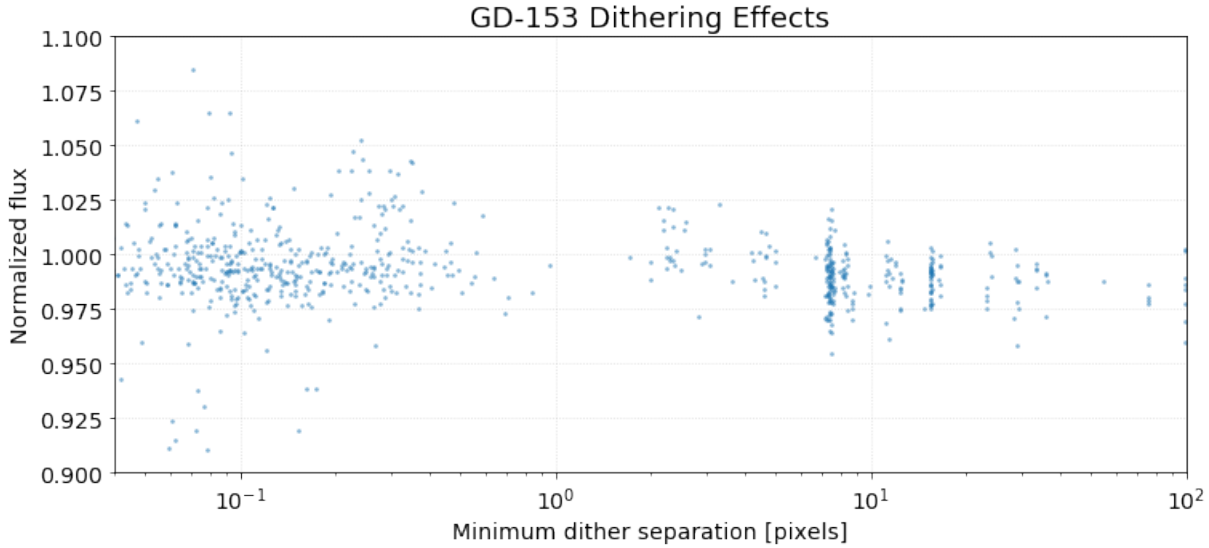

Figure 8: Normalized photometry of the standard star GD-153 as a function of dither separation. The values were normalized to the median measured flux in the corresponding filter. The loose clustering of points at $x < 1$ represent undithered data, and the spread is due to centroid uncertainty.

As shown in Figure 8, the non or minimally dithered data shows a slightly higher photometric dispersion than points with larger dithers. The median and standard deviation of the normalized photometry with dither separation less than 10 pixels are 1.001 and 0.014 (1.4%) respectively. For the points with a dither separation greater than 10 pixels, the values are 0.996 and 0.09 (0.9%) respectively. The less than unity flux calculated for the larger dither values is indicative of a mitigation of persistence (persistence would make the sources appear brighter). Since the majority of observations were taken with dithers too small to mitigate

persistence, the median of all the measurements (a value of 1.00 on the y axis) is biased to be brighter. The higher standard deviation of the observations with dither separations of less than 10 pixels is also due to persistence, as persistence does not affect (brighten) the first exposures in a visit as strongly as the later exposures. This causes a larger spread in the measurements. Since the larger dither separations are not affected by persistence, the spread is lower.

Large Dithers

The lower standard deviation (better repeatability) of observations with large dither separations shown in Figure 8 can be observed in the measurements of CB-130 as well. The photometric measurements from exposures of CB130 in fresh dither positions (the lowest four points in Figure 5) show little to no systematic increase over the course of the visit, indicating that those measurements suffer from virtually no persistence effects. Reproducing Figure 2 only including the measurements from exposures not affected by persistence shows a remarkable improvement in the standard deviation:

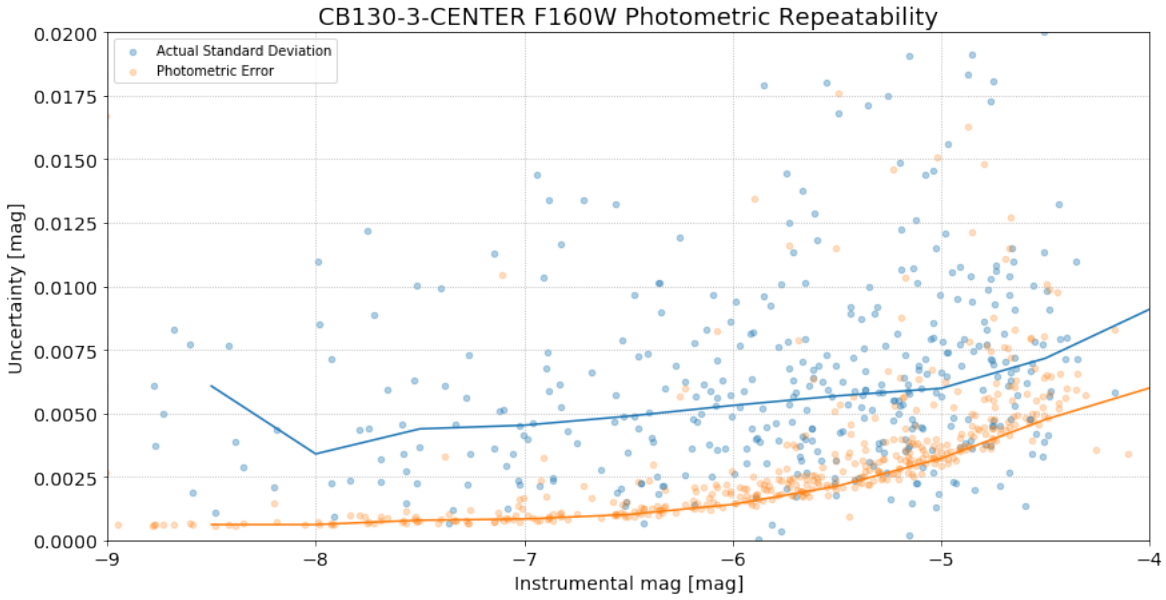

Figure 9: Comparison of the median photometric error and the standard deviation of measurements in CB130 as a function of instrumental magnitude, only using the measurements from exposures unaffected by persistence. The blue points are the standard deviation of the measurements, and the orange are the median of the photometric error. The solid lines are the medians in half-magnitude bins.

The standard deviation of the photometric measurements for almost all the stars is less than 1%, with an average value of approximately 0.5% (but increases to 0.6% when Poisson noise becomes non-negligible as in the fainter end here) , three times smaller than when including persistence-affected images.

Flat-field Errors

While persistence causes a loss in precision, photometric measurements still show scatter larger than Poisson noise when dithers are large enough to avoid persistence. As a result of dithering, sources land on different detector positions, so part of the noise may be due to errors in the flat-field. The reported error of the flat-field is reported to be approximately 0.5% rms in Pirzkal et al. (2011), however this increases to approximately 0.8% in the areas less than 128 pixels from the edge of the detector.

If the flat-field errors had some spatial dependence (aside from the edges being more noisy), then photometric measurements with larger dithers should have larger scatter. However, an analysis performed in Dahlen (2013) shows that dithering a single source to 42 different points all across the detector and performing photometry results in an rms of approximately 0.7%. It should be noted that these measurements cover the edges of the detector (where the flat-fields are known to be noisy), and the Poisson noise of some of these measurements is larger (up to 0.6% for the shortest observations). Thus, these measurements are very nearly consistent with the 0.5% seen in figure 9, indicating that dithers of tens of pixels produce similar (or only marginally better) results to dithers of hundreds of pixels, whilst withing the inner 800x800 pixels of the detector.

If the errors in the flat-field were smaller over distances of only a few pixels, then smaller dithers may mitigate some of the photometric noise, however figure 4 shows that these observations would be contaminated by persistence, which would result in even larger errors. Thus, it is unknown if the flat-field errors are smaller over distances of a few pixels.

If no dithers are performed then photometric precision is not affected by the flat-field, however persistence generally affects these measurements much more strongly. It is possible that the effect of persistence levels off after a large number of undithered exposures (see the rightmost points in figure 6). The last four exposures in Visit 06 in program 11933 (the last four red triangles in figure 6) show a somewhat better repeatability (standard deviation) of 0.35%. This indicates that some of the error in the dithered data is likely from the flat-fields. **However, that is not to say we recommend not dithering for photometric observations**, as there are many caveats with these measurements and therefore the computed repeatability level. The measured count rates are a combination of the actual flux incident upon the detector, as well as the persistence signal, and so the accuracy of the measurements is worse than measurements unaffected by persistence. Furthermore, the persistence signal levels off only after a large amount of preceding exposures in the same dither position, and is only obtainable with large amounts of observation time (and even then, is likely still inaccurate). Lastly, dithering also mitigates the effects of bad pixels, and can give better subsampling of the PSF. In almost all cases **we strongly advise against this observation strategy**.

Conclusions

The effects of persistence systematically increase the apparent brightness of sources from exposure to exposure, making the standard deviation of repeated photometric measurements artificially increase. The standard deviation for typical stellar observations affected by per-

sistence is 0.01 - 0.015 magnitudes (1-1.5%) on average. However, the stars in an exposure strongly affected by persistence can be on **average** (an individual star may have an even larger range) 0.02 - 0.03 magnitudes brighter than the same stars in an unaffected exposure (dependent on time since and measured fluence of the persistence causing image/source).

While dithering often mitigates persistence from the brightest pixel of sources, the wings of the PSF can also cause significant persistence, especially when the source is bright or the previous exposures were long (as both conditions cause a higher total fluence), as shown in the measurements of M4 (figure 4). Thus, many of the standard dither patterns, such as `WFC3-IR-DITHER-BOX-MIN` which has a spacing of 4.5 pixels, do not have a large enough spacing between dither positions to ensure pixels falling within a photometric aperture (of which the standard is a radius of 3 pixels) are unaffected by persistence.

The comparisons of figures 9 and 2 shows that repeatability of persistence-free photometric measurements is substantially better. While not quite as precise as the theoretical photon limited case, the 1σ repeatability is .5%, substantially better than the original 1.5%. This is representative of the noise floor of the calibration of WFC3/IR, and is the approximate limit of the precision of aperture photometry measurements. This is further supported by the measurements of the standard star GD-153, which show measurements with larger dithers having a standard deviation of just under 1% (of which Poisson/background error was calculated to be about 0.5%). A portion of the 0.5% noise floor is likely due to small errors in the flat-field. These errors seem to be fairly uniform in the central 800x800 pixels of the detector, but increase towards the edges of the array.

If high precision photometric measurements are desired, an observation strategy consisting of larger, frequent dithers is likely required. While the observations of CB130 are dithered by approximately 60 pixels to mitigate persistence, a smaller distance would likely achieve similar results due to the small size of the WFC/IR PSF. As such, **we recommend a dither of at least 10 pixels to avoid persistence effects on photometric measurements**. Ideally, the frequency of the dithers would be after each exposure, with each dither position in a new, previously unused position, though this incurs a larger amount of overhead in the observations. This may not be possible in extremely crowded fields, as the high number of stars would leave only a small amount of "fresh" pixels that are free of persistence. If using multiple filters in contemporaneous observations, arranging lower total fluence images **before** those with larger fluences (i.e. narrow band before wide band filters, or short before long exposures) can also mitigate persistence effects when dithering is undesirable.

Larger dithers have been used in the calibration programs observing the standard stars. The effects of this updated observing strategy can be seen in figure 7. The points located at $x > 58000$ show a slightly smaller scatter than those to the left, likely due to the lack of persistence. The increase in precision from persistence mitigation will allow for more accurate analysis and computation of the photometric zeropoints.

Acknowledgements

We thank A. Calamida, H. Khandrika, J. Mack, J. Medina, and S. Deustua of the WFC3 Photometry Calibration group and E. Sabbi for their suggestions regarding analysis contained in and clarity of this report. We also thank Professor Adam Riess for his review of

this document.

References

Bajaj, V. (2017). *Aligning HST Images to Gaia: a Faster Mosaicking Workflow*. WFC3 ISR 2017-19.

Bradley, Larry et al. (2017). *astropy/photutils: v0.4*. DOI: 10.5281/zenodo.1039309. URL: https://doi.org/10.5281/zenodo.1039309.

Dahlen, T. (2013). *WFC3/IR Spatial Sensitivity Test*. WFC3 ISR 2013-01.

Long, K., S. Baggett, and V. Kozhurina-Platais (2016). *The Effect of Repeated Exposures on Measured Fluxes in the WFC3/IR Detector*. WFC3 ISR 2016-11.

Pirzkal, N. et al. (2011). *Sky Flats: Generating Improved WFC3 IR Fale-fields*. WFC3 ISR 2011-11.

The Astropy Collaboration et al. (2018). "The Astropy Project: Building an inclusive, open-science project and status of the v2.0 core package". In: *ArXiv e-prints*. arXiv: 1801.02634 [astro-ph.IM].

Appendices

A Target Information

In this section we present further information about the exposures used in the analysis of the various targets. This information contains mainly observational parameters, such as the exposure times and dithering information.

CB130

The observations of CB130 were taken in a two-orbit visit using the F160W filter as part of HST GO Program 11618. The images were taken in groups of 3 followed by a large, box-like dither of approximately 60 pixels. The exposures in each group were taken with decreasing exposure times, the first was long, then a medium, and then a short exposure. Further details are in the figures/tables below.

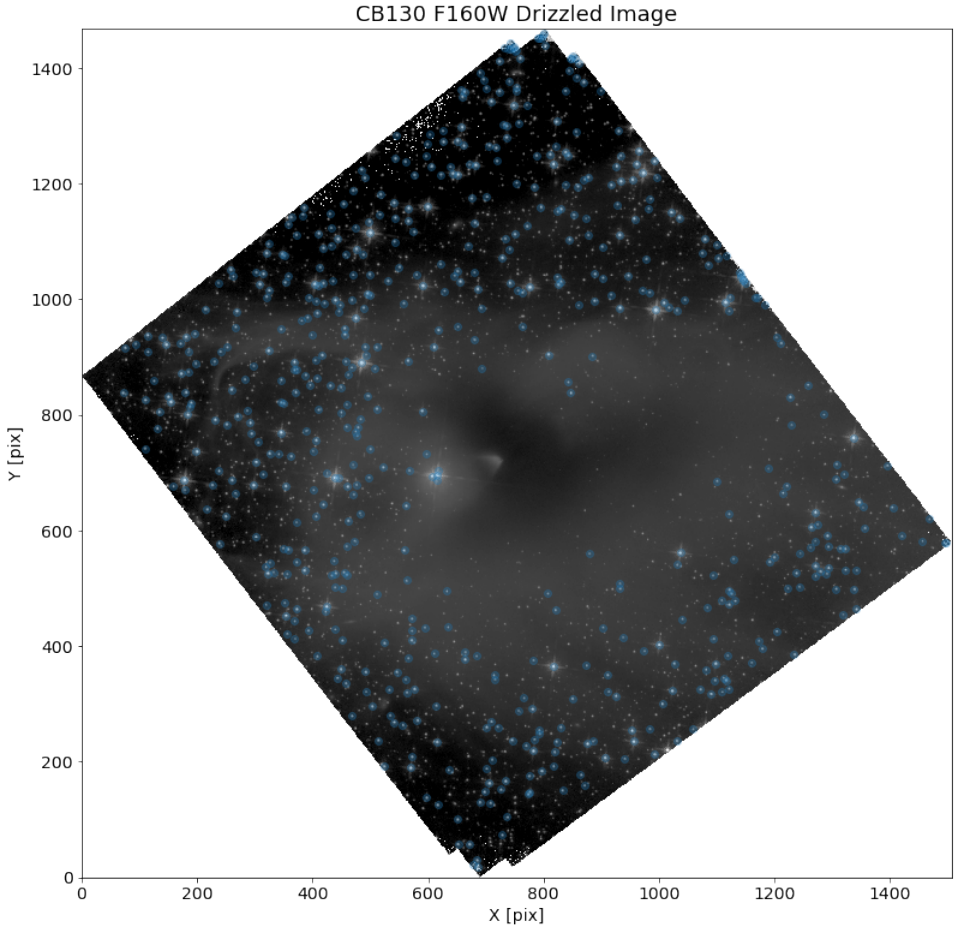

Figure 10: The F160W drizzled image of CB130. North is aligned with the Y axis. The field contains many stars, but is not overcrowded. Approximately 500 sources were used in this analysis and are marked with blue circles.

Filename	Filter	Exptime	Date-Obs	Time-Obs	Sample Sequence	N Samp
ib6302ipq_flt.fits	F160W	24.229715	2009-10-13	07:46:49	STEP100	6
ib6302i1q_flt.fits	F160W	899.233093	2009-10-13	06:14:48	STEP100	16
ib6302hyq_flt.fits	F160W	399.231567	2009-10-13	06:05:44	STEP100	11
ib6302hxq_flt.fits	F160W	899.233093	2009-10-13	05:50:24	STEP100	16
ib6302inq_flt.fits	F160W	499.231873	2009-10-13	07:38:09	STEP100	12
ib6302i0q_flt.fits	F160W	49.230225	2009-10-13	06:12:44	STEP100	7
ib6302i3q_flt.fits	F160W	399.231567	2009-10-13	06:30:08	STEP100	11
ib6302ilq_flt.fits	F160W	899.233093	2009-10-13	07:22:49	STEP100	16
ib6302isq_flt.fits	F160W	499.231873	2009-10-13	08:03:43	STEP100	12
ib6302iqq_flt.fits	F160W	899.233093	2009-10-13	07:48:23	STEP100	16
ib6302i5q_flt.fits	F160W	49.230225	2009-10-13	06:37:08	STEP100	7
ib6302itq_flt.fits	F160W	24.229715	2009-10-13	08:12:23	STEP100	6

Table 2: Details of the exposures of CB130. Note the occultation period between the sixth and seventh exposures.

Filename	RA_Aper	Dec_Aper	Postarg1	Postarg2
ib6302hxq_flt.fits	274.0659	-2.5443	-5.407	-4.832
ib6302hyq_flt.fits	274.0659	-2.5443	-5.407	-4.832
ib6302i0q_flt.fits	274.0659	-2.5443	-5.407	-4.832
ib6302i1q_flt.fits	274.0699	-2.5435	5.407	4.832
ib6302i3q_flt.fits	274.0699	-2.5435	5.407	4.832
ib6302i5q_flt.fits	274.0699	-2.5435	5.407	4.832
ib6302ilq_flt.fits	274.0678	-2.5429	2.704	-2.416
ib6302inq_flt.fits	274.0678	-2.5429	2.704	-2.416
ib6302ipq_flt.fits	274.0678	-2.5429	2.704	-2.416
ib6302iqq_flt.fits	274.068	-2.5449	-2.704	2.416
ib6302isq_flt.fits	274.068	-2.5449	-2.704	2.416
ib6302itq_flt.fits	274.068	-2.5449	-2.704	2.416

Table 3: The pointings of the CB130 exposures. Groups of three exposures were taken at the same position.

Messier 4

The observations of M4 were taken in a four-orbit visit using the F160W filter as part of HST GO Program 12602. Each orbit consisted of four medium length exposures with the `WFC3-IR-DITHER-BOX-MIN` pattern used after each exposure, resulting in the position same being used in the following orbit. Further details are in the figures/tables below.

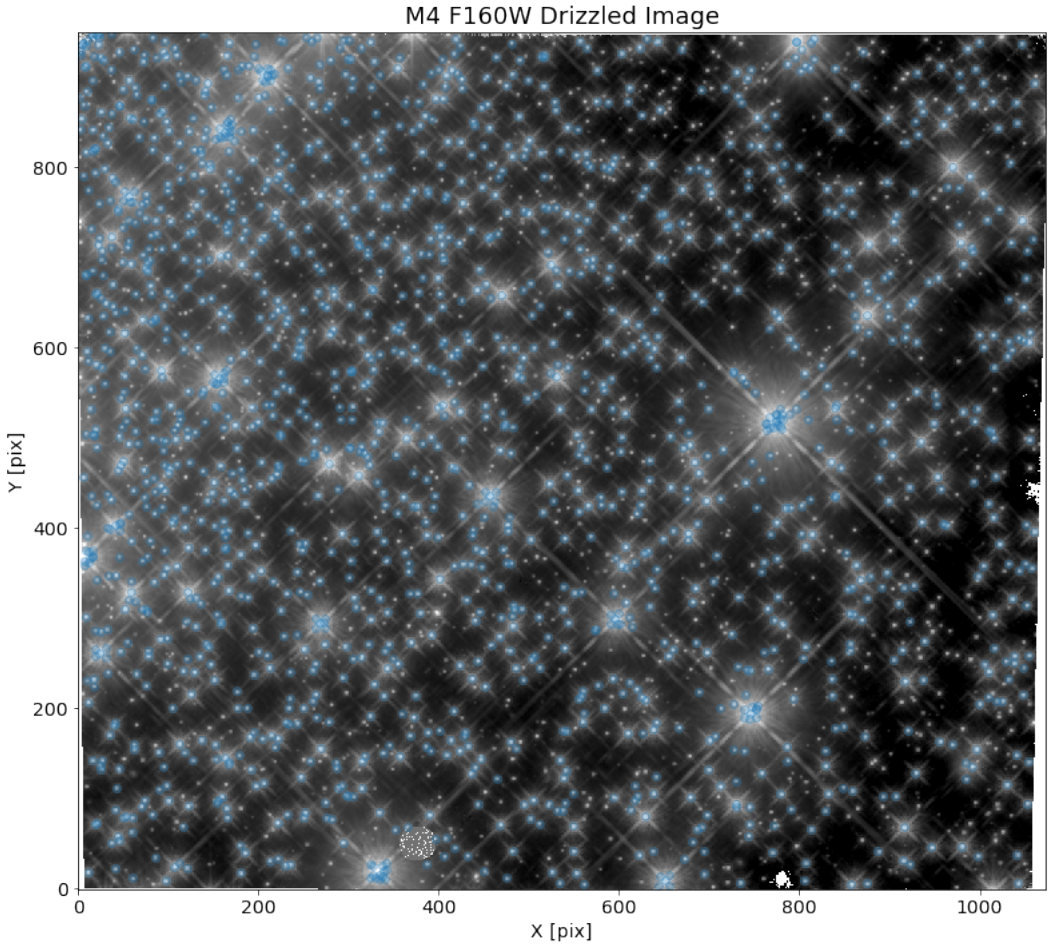

Figure 11: The F160W drizzled image of M4. While the center of the cluster is likely too crowded for this analysis, the IR images were taken in the outer regions, where the crowding is less. Approximately 1500 sources were used in this analysis and are marked with blue circles.

Filename	Filter	Exptime	Date-Obs	Time-Obs	Sample Sequence	N Samp
ibqj02gfq_flt.fits	F160W	652.937744	2012-04-20	20:46:09	SPARS50	15
ibqj02giq_flt.fits	F160W	652.937744	2012-04-20	20:58:04	SPARS50	15
ibqj02gmq_flt.fits	F160W	652.937744	2012-04-20	21:09:59	SPARS50	15
ibqj02gqq_flt.fits	F160W	652.937744	2012-04-20	21:21:54	SPARS50	15
ibqj02guq_flt.fits	F160W	652.937744	2012-04-20	22:21:28	SPARS50	15
ibqj02gyq_flt.fits	F160W	652.937744	2012-04-20	22:33:23	SPARS50	15
ibqj02h2q_flt.fits	F160W	652.937744	2012-04-20	22:45:18	SPARS50	15
ibqj02h6q_flt.fits	F160W	652.937744	2012-04-20	22:57:13	SPARS50	15
ibqj02haq_flt.fits	F160W	652.937744	2012-04-20	23:57:39	SPARS50	15
ibqj02hhq_flt.fits	F160W	652.937744	2012-04-21	00:09:34	SPARS50	15
ibqj02hlq_flt.fits	F160W	652.937744	2012-04-21	00:21:29	SPARS50	15
ibqj02hpq_flt.fits	F160W	652.937744	2012-04-21	00:33:24	SPARS50	15
ibqj02hyq_flt.fits	F160W	652.937744	2012-04-21	01:28:00	SPARS50	15
ibqj02i2q_flt.fits	F160W	652.937744	2012-04-21	01:39:55	SPARS50	15
ibqj02i6q_flt.fits	F160W	652.937744	2012-04-21	01:51:50	SPARS50	15
ibqj02iaq_flt.fits	F160W	652.937744	2012-04-21	02:03:45	SPARS50	15

Table 4: Details of the exposures of M4. Note the occultation period after each group of four exposures.

Filename	RA_Aper	Dec_Aper	Postarg1	Postarg2
ibqj02gfq_flt.fits	245.9238	-26.5053	0.0	0.0
ibqj02giq_flt.fits	245.9236	-26.5053	0.542	0.182
ibqj02gmq_flt.fits	245.9237	-26.5052	0.339	0.485
ibqj02gqq_flt.fits	245.9238	-26.5052	-0.203	0.303
ibqj02guq_flt.fits	245.9238	-26.5053	0.0	0.0
ibqj02gyq_flt.fits	245.9236	-26.5053	0.542	0.182
ibqj02h2q_flt.fits	245.9237	-26.5052	0.339	0.485
ibqj02h6q_flt.fits	245.9238	-26.5052	-0.203	0.303
ibqj02haq_flt.fits	245.9238	-26.5053	0.0	0.0
ibqj02hhq_flt.fits	245.9236	-26.5053	0.542	0.182
ibqj02hlq_flt.fits	245.9237	-26.5052	0.339	0.485
ibqj02hpq_flt.fits	245.9238	-26.5052	-0.203	0.303
ibqj02hyq_flt.fits	245.9238	-26.5053	0.0	0.0
ibqj02i2q_flt.fits	245.9236	-26.5053	0.542	0.182
ibqj02i6q_flt.fits	245.9237	-26.5052	0.339	0.485
ibqj02iaq_flt.fits	245.9238	-26.5052	-0.203	0.303

Table 5: The pointings of the M4 exposures. The same four positions were used across all four orbits

NGC 1850

The observations of NGC1850 were taken in 3 separate CVZ orbits and were not dithered (and as such the table detailing the pointings is excluded). The observations were taken in both F110W and F160W, and both filters are used in the analysis. Further details are in the figures/tables below.

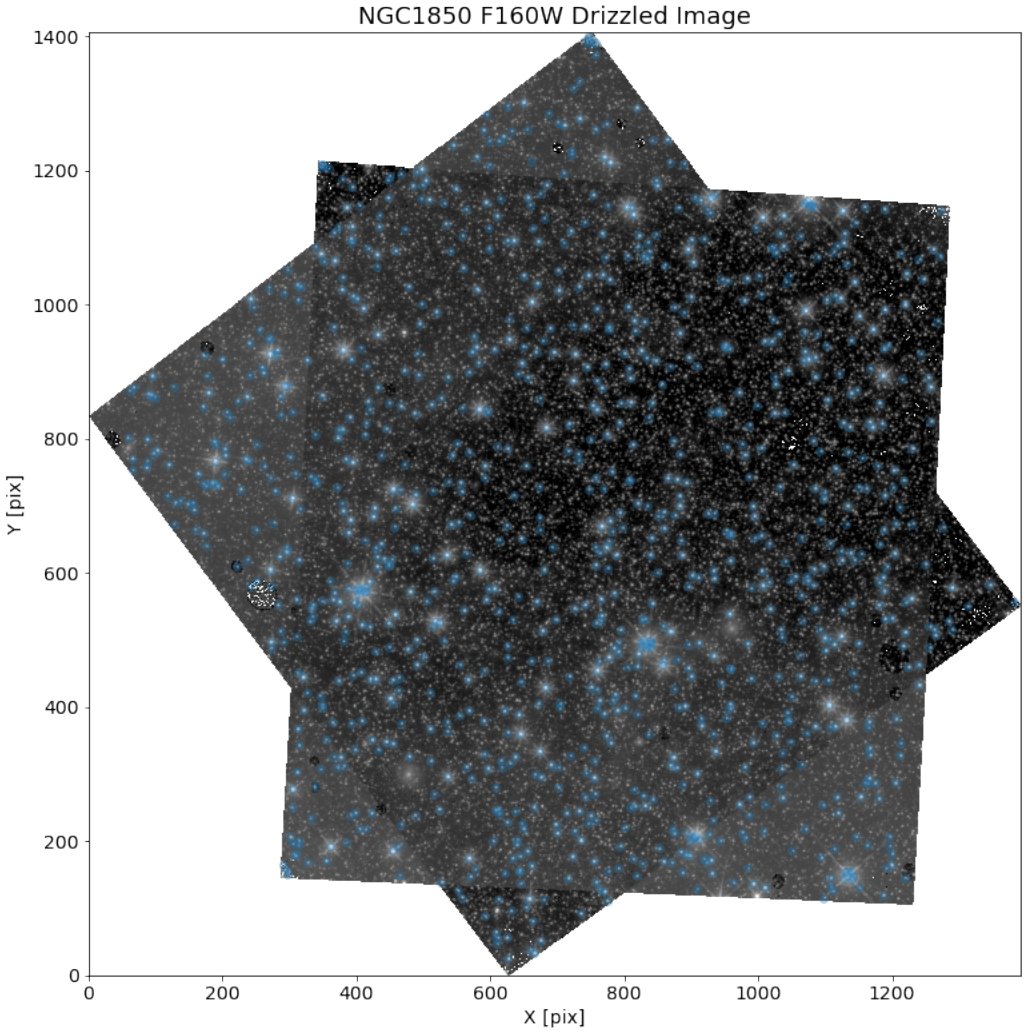

Figure 12: The F160W drizzled image of NGC 1850. While the center of the cluster is likely too crowded for this analysis, the IR images were taken in the outer regions, where the crowding is less. Approximately 2000 sources were used in this analysis and are marked with blue circles.

Filename	Filter	Exptime	Date-Obs	Time-Obs	Sample Sequence	N Samp
ibaq01kfq_flt.fits	F110W	252.934357	2010-07-27	09:34:41	SPARS50	7
ibaq01kgq_flt.fits	F110W	252.934357	2010-07-27	09:39:15	SPARS50	7
ibaq01kiq_flt.fits	F110W	252.934357	2010-07-27	09:43:49	SPARS50	7
ibaq01kkq_flt.fits	F110W	252.934357	2010-07-27	09:48:23	SPARS50	7
ibaq01klq_flt.fits	F110W	252.934357	2010-07-27	09:52:57	SPARS50	7
ibaq01knq_flt.fits	F110W	252.934357	2010-07-27	09:57:31	SPARS50	7
ibaq01kpq_flt.fits	F110W	252.934357	2010-07-27	10:02:05	SPARS50	7
ibaq01krq_flt.fits	F110W	252.934357	2010-07-27	10:06:39	SPARS50	7
ibaq01ksq_flt.fits	F110W	252.934357	2010-07-27	10:11:13	SPARS50	7
ibaq01kuq_flt.fits	F110W	252.934357	2010-07-27	10:15:47	SPARS50	7
ibaq01kwq_flt.fits	F110W	252.934357	2010-07-27	10:20:21	SPARS50	7
ibaq01kyq_flt.fits	F110W	252.934357	2010-07-27	10:24:55	SPARS50	7
ibaq01kzq_flt.fits	F110W	252.934357	2010-07-27	10:29:29	SPARS50	7
ibaq01l1q_flt.fits	F110W	252.934357	2010-07-27	10:34:03	SPARS50	7
ibaq01l3q_flt.fits	F110W	252.934357	2010-07-27	10:38:37	SPARS50	7
ibaq01l5q_flt.fits	F110W	252.934357	2010-07-27	10:43:11	SPARS50	7
ibaq01l6q_flt.fits	F110W	252.934357	2010-07-27	10:47:45	SPARS50	7
ibaq01l7q_flt.fits	F110W	252.934357	2010-07-27	10:52:19	SPARS50	7
ibaq01l8q_flt.fits	F110W	252.934357	2010-07-27	10:56:53	SPARS50	7
ibaq02ylq_flt.fits	F160W	252.934357	2010-07-23	11:27:19	SPARS50	7
ibaq02ymq_flt.fits	F160W	252.934357	2010-07-23	11:31:53	SPARS50	7
ibaq02yoq_flt.fits	F160W	252.934357	2010-07-23	11:36:27	SPARS50	7
ibaq02yqq_flt.fits	F160W	252.934357	2010-07-23	11:41:01	SPARS50	7
ibaq02yrq_flt.fits	F160W	252.934357	2010-07-23	11:45:35	SPARS50	7
ibaq02ytq_flt.fits	F160W	252.934357	2010-07-23	11:50:09	SPARS50	7
ibaq02yvq_flt.fits	F160W	252.934357	2010-07-23	11:54:43	SPARS50	7
ibaq02yxq_flt.fits	F160W	252.934357	2010-07-23	11:59:17	SPARS50	7

Table 6: Details of the exposures of NGC1850. Exposures were generally taken in 3 separate multi-orbit visits. Since this target is located in the CVZ, there is no occultation period, enabling an uninterrupted, continuous sequence of many exposures. Images taken within the same visit were not dithered.

Filename	Filter	Exptime	Date-Obs	Time-Obs	Sample Sequence	N Samp
ibaq02yyq_flt.fits	F160W	252.934357	2010-07-23	12:03:51	SPARS50	7
ibaq02z0q_flt.fits	F160W	252.934357	2010-07-23	12:08:25	SPARS50	7
ibaq02z2q_flt.fits	F160W	252.934357	2010-07-23	12:12:59	SPARS50	7
ibaq02z4q_flt.fits	F160W	252.934357	2010-07-23	12:17:33	SPARS50	7
ibaq02z5q_flt.fits	F160W	252.934357	2010-07-23	12:22:07	SPARS50	7
ibaq02z7q_flt.fits	F160W	252.934357	2010-07-23	12:26:41	SPARS50	7
ibaq02z9q_flt.fits	F160W	252.934357	2010-07-23	12:31:15	SPARS50	7
ibaq02zbq_flt.fits	F160W	252.934357	2010-07-23	12:35:49	SPARS50	7
ibaq02zcq_flt.fits	F160W	252.934357	2010-07-23	12:40:23	SPARS50	7
ibaq02zdq_flt.fits	F160W	252.934357	2010-07-23	12:44:57	SPARS50	7
ibaq02zeq_flt.fits	F160W	252.934357	2010-07-23	12:49:31	SPARS50	7
ibaq06u7q_flt.fits	F160W	252.934357	2011-03-05	17:23:06	SPARS50	7
ibaq06u8q_flt.fits	F160W	252.934357	2011-03-05	17:27:40	SPARS50	7
ibaq06uaq_flt.fits	F160W	252.934357	2011-03-05	17:32:14	SPARS50	7
ibaq06ucq_flt.fits	F160W	252.934357	2011-03-05	17:36:48	SPARS50	7
ibaq06udq_flt.fits	F160W	252.934357	2011-03-05	17:41:22	SPARS50	7
ibaq06ufq_flt.fits	F160W	252.934357	2011-03-05	17:45:56	SPARS50	7
ibaq06uhq_flt.fits	F160W	252.934357	2011-03-05	17:50:30	SPARS50	7
ibaq06ujq_flt.fits	F160W	252.934357	2011-03-05	17:55:04	SPARS50	7
ibaq06ukq_flt.fits	F160W	252.934357	2011-03-05	17:59:38	SPARS50	7
ibaq06umq_flt.fits	F160W	252.934357	2011-03-05	18:04:12	SPARS50	7
ibaq06uoq_flt.fits	F160W	252.934357	2011-03-05	18:08:46	SPARS50	7
ibaq06uqq_flt.fits	F160W	252.934357	2011-03-05	18:13:20	SPARS50	7
ibaq06urq_flt.fits	F160W	252.934357	2011-03-05	18:17:54	SPARS50	7
ibaq06utq_flt.fits	F160W	252.934357	2011-03-05	18:22:28	SPARS50	7
ibaq06uvq_flt.fits	F160W	252.934357	2011-03-05	18:27:02	SPARS50	7
ibaq06uwq_flt.fits	F160W	252.934357	2011-03-05	18:31:36	SPARS50	7
ibaq06uxq_flt.fits	F160W	252.934357	2011-03-05	18:36:10	SPARS50	7

Table 7: [Continuation of Table 6] Details of the exposures of NGC1850. Exposures were generally taken in 3 separate multi-orbit visits. Since this target is located in the CVZ, there is no occultation period, enabling an uninterrupted, continuous sequence of many exposures. Images taken within the same visit were not dithered.

GD-153

All available WFC3/IR imaging observations (947 images) of the spectrophotomertric standard star GD-153 were used in this analysis. The full complement of the 15 WFC3/IR imaging filters were used in these observations. Many different exposure times, sample sequences, NSAMPS, apertures, and dithers were used, as the observations were taken as parts of several programs. The observations were taken in the following programs:

CAL: 11451, 11552, 11926, 12334, 12699, 12702, 13089, 13092 , 13575, 13579, 14021, 14384, 14386, 14544,14883, 14992, 14994, and 15582. GO: 13711 and 15113.